In-beam Performance of the ALICE Silicon-Strip Detectors

F. Agnese [c] F. Benedosso [a,d,e] D. Bonnet [c] V.N. Borshchov [g]
O. Borysov [f] L. Bosisio [d,e] M. Bregant [d,e] A. van den Brink [a]
P. Camerini [d,e] G.Contin [e] E. Fragiacomo [e] C. Gojak [c] N. Grion [e]
R. Grosso [d,e] A.P. de Haas [a] S.N. Igolkine [j] S.K. Kiprich [g]
R.Kluit [b] C. Kuhn [c] P.G. Kuijer [a,b] O.M. Listratenko [g]
J.R. Lutz [c] G.V. Margagliotti [d,e] G.J.L. Nooren [a,b] M. Oinonen [h]
C.J. Oskamp [a] W.Peryt [k] S. Piano [d,e] S. Plumeri [c] Z. Radiojevic [i]
I. Rashevskaya [e] R. Rui [d,e] J.D.Schippers [b] H. Seppänen [h]
O. Sokolov [a,*] M.Szuba [k] P.Timmer [b] G. Zinovjev [f]

[a] *Utrecht University, The Netherlands*

[b] *NIKHEF, The Netherlands*

[c] *Institut de Recherches Subatomiques-IReS, IN2P3/CNRS and ULP, France*

[d] *Dipartimento di Fisica, Università di Trieste, Italy*

[e] *Istituto Nazionale di Fisica Nucleare (INFN), Sezione di Trieste, Italy*

[f] *Bogolyubov Institute for Theoretical Physics, Kiev, Ukraine*

[g] *Scientific and Technological Research Institute of Instrument Engeneering, Kharkov, Ukraine*

[h] *Helsinki Institute of Physics, University of Helsinki, Helsinki, Finland*

[i] *Nokia Research Center, Helsinki, Finland*

[j] *CERN, Geneva, Switzerland*

[k] *Warsaw University of Technology, Faculty of Physics, Poland*

Abstract

This paper presents the beam test results of the first four double-sided silicon strip modules built for the inner tracker of ALICE detector. The basic detector performance was studied with the focus made on the efficiency and spatial resolution determination. A fast method for the determination of the spatial resolution of the sensors in the telescope is described.

Key words: Double-sided AC silicon strip detector, Particle telescope, Spatial resolution, Efficiency, ALICE ITS

Preprint submitted to Nuclear Instruments and Methods A *3 January 2006*

1 Introduction

The inner tracker system (ITS) [1,2] of ALICE [3] experiment consists of six cylindrical layers of silicon detectors. The silicon strip detectors (SSD) comprise the outer two layers of ITS and play an important role in matching the particle tracks found by ITS to the TPC tracks and in particle identification by ITS.

The SSD layers are constructed from 1698 SSD modules, each containing a 75×42 mm^2 double-sided 300 μm thick silicon strip sensor. The strip pitch is 95 μm on both sides, with 768 strips per side. On one side the strips are tilted by an angle of 7.5 mrad with respect to the short edge of the sensor and on the other side by an angle of 27.5 mrad creating a stereo angle of 35 mrad so that each strip crosses only 15 strips of the opposite side. This allows to reconstruct multiple hits from the same sensor at the expense of the poorer spatial resolution in the direction along the sensor shorter edge (z direction in ALICE frame) while keeping fine resolution in $r\phi$ direction (along the longer edge) for better particle momentum resolution. The bulk of the sensor is n-type silicon with p^+ type implanted strips on one side (P-side) and n^+ type silicon strips on the other side (N-side) insulated by p^+ doped region. Integrated capacitors on top of each strip enable AC coupling to the front end, providing separation of the leakage current in the strips from the inputs of readout electronics [1]. The sensor is biased by a punch-through structure [4]. The sensors are produced by three different manufacturers, each implementing the sensor in a slightly different way. The differences relevant in this context are the strip widths: 40 μm (ITC[1]), 26 μm (SINTEF[2]) and 45 μm (CANBERRA[3]). Each side of the sensor is connected to a hybrid circuit carrying 6 HAL25[4] read-out chips[5] each. The readout pitch is the same as the strip pitch. The 128-channel front-end chips amplify and shape the signals from the sensor and contain a sample-hold circuit to store the analogue signal after a trigger. The analog samples can be read-out serially at speeds up-to 10^6 samples per second. The peaking time of the shaping circuit is adjustable between 1.4 μs and 2.2 μs . All parameters of the front-end chips are controlled via a JTAG interface. Connections on the hybrid and

---

[*] Corresponding author, Tel.: +31-(0)30-253-9462; fax: +31-(0)30-251-8689
Email address: `O.Sokolov@phys.uu.nl` (O. Sokolov).

[1] Manufactured by ITC-IRST, Italy

[2] Manufactured by SINTEF, Norway

[3] Manufactured by CANBERRA EURISYS, France

[4] Manufactured by IBM, USA.

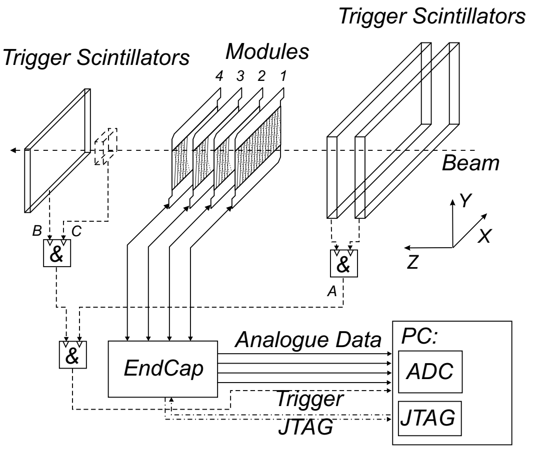

Fig. 1. Schematic layout of the beam test set-up. The four modules under test were surrounded by the trigger scintillators A,B and C.

the connections between the front-end chips and the sensor are made using micro-cables consisting of aluminium conductors on a polymer carrier[6]. The hybrids are connected to the EndCap boards which decouple the analog and control signals from the sensor bias voltage and buffer all signals to and from the front-end chips and generate the control signals for read-out of the analog buffers using two ASICs[7].

The first four prototype SSD modules corresponding to the final design were tested using a secondary 7 GeV/c pion beam produced at the CERN PS accelerator. This paper presents the major detector performance results obtained during this beam test. In the Section 2 the description of the beam test setup is given, Section 3 gives extensive details on the off-line analysis and the Section 4 summarizes the obtained results.

2 Experimental Set-up

A schematic view of the set-up is shown in figure 1. Four modules were arranged in a telescope with a spacing of 3 cm between the sensors. No external telescope was used. The incident beam traversed the sensors normal to the surface and was centered in the middle of the sensors, covering almost the entire sensor area. Every particle spill delivered about 5000 pions in 0.6 s, with 16 s gap between the spills. The trigger signals were produced from the coincidence of four plastic scintillators. Scintillator B, about 8×5 cm^2, was placed downstream with respect to the modules. The two scintillators A, placed upstream in the beam, were $20 \times 25 \times 1$ cm^3, with a gap of 6 cm between them. Another small scintillator covering roughly 1/6 of the sensor allowed the selection of a fraction of the sensor area. The hybrids were connected to the prototype EndCap boards. The EndCap boards were connected to a data acquisition system consisting of a four channel 12-bit ADC[5] board in a PC running Labview. The sampling frequency of the ADC card was set to 10 MHz, corresponding to the nominal read-out speed of the front-end modules. The maximum trigger rate that the system could accept was about 100 Hz. The preliminary hit reconstruction was performed in between the particle spills (every 16 seconds) and the information on the hit locations and deposited charge was displayed online for monitoring purposes. JTAG interface to the front-end chips and EndCaps was done using a boundary scan controller[6].

3 Off-line analysis

3.1 Cluster finding

The initial pedestals and noise were calculated from the first 1000 events of a particle run. The pedestals were continuously updated during the run using a “moving window” method to track the pedestal drift. After the pedestal and common mode subtraction one obtains the signals S_i proportional to the charge collected by the i-th strip. Strips with $(S_i/N_i) > 3$ are qualified as fired strips, where N_i is the noise of the i-th strip. Contiguous fired strips are combined into a cluster, disconnected strips (i.e. due to a bonding failure) that collect no charge are included in the cluster if they are in between two other fired strips. Only clusters with $S_{Cl}/N_{Cl} > 5$ are kept, where $S_{Cl} = \sum_i^n S_i$ is the total cluster charge and

$$N_{Cl} = \sqrt{\sum_{ij}^{n} \rho_{ij} \cdot N_i N_j} \tag{1}$$

is the total cluster noise calculated including the noise correlation coefficients ρ_{ij} between the strips i and j. The cluster position (in pitch units) is determined using a center of gravity (COG) algorithm:

$$\langle i \rangle_{COG} = \frac{\sum_i^n i \cdot S_i}{\sum_i^n S_i} \tag{2}$$

where the i’s are the indices of the strips included in the cluster. This procedure is done independently for both sensor sides. Two clusters found on opposite sides are associated with a particle hit if the fired strips on one side have a point of intersection with the fired strips on the other side. If more then one cluster per side is found, then as long as the distance between the cluster centers on the same side is more than 15 strips, no ambiguity emerges, otherwise

---

[5] ADC DAS 4020/12 card manufactured by Measurementcomputing .

[6] PM 3705 manufactured by Philips

the ambiguity is resolved by keeping only the combination with the best P-N charge match [1]. All the analysis in this paper was done using the events with at most one hit per sensor. The information on the cluster position from both sides is used to calculate the hit cartesian coordinates (x, y).

3.2 Cluster size and charge

The histogram of the relative number of clusters having 1, 2, 3 or more strips in the cluster is shown on fig. 2 for all four modules. For this figure only the clusters not adjacent to disconnected strips were selected. Due to a large strip pitch compared to the diffusion width of the generated charge cloud, there is a significant fraction of single strip clusters on all the modules. The single-strip clusters give no opportunity to use any charge sharing model to determine the position of those clusters with a better precision. A high strip noise seen on the N-side of modules 1 and 2 (see tab.1) increases the number of such clusters even more since the high noise masks the charge collected due to the carrier diffusion and capacitive coupling by the strips adjacent to the strip that collects the most of the charge.

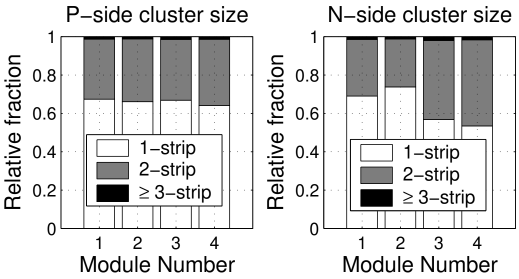

Fig. 2. Cluster size histogram at normal incidence.

The histogram of the cluster charge collected by both P and N sides of module 4 is shown on fig.3. Only events with clusters not adjacent to disconnected and very noisy strips were used. The position of the peak corresponds to the most probable charge deposition by beam particles, assumed equal to 25000 e^- [8]. This value in ADC counts is slightly different for P and N sides due to a different capacitive networks on the two sides and/or a different gain of the front end electronics for signals of the opposite polarity. The histogram is fitted with a Landau curve convoluted with a Gaussian function:

$$f(x, \Delta) = 1/\sqrt{2\pi\sigma^2} \int_{-\infty}^{+\infty} f_L(x, \Delta') \times \exp[-(\Delta - \Delta')^2/2\sigma^2] \mathrm{d}\Delta' \quad (3)$$

where Δ is the actual energy loss when a distance x is traversed, and $f_L(x, \Delta)$ is the Landau distribution function [9]. This is necessary to account for the

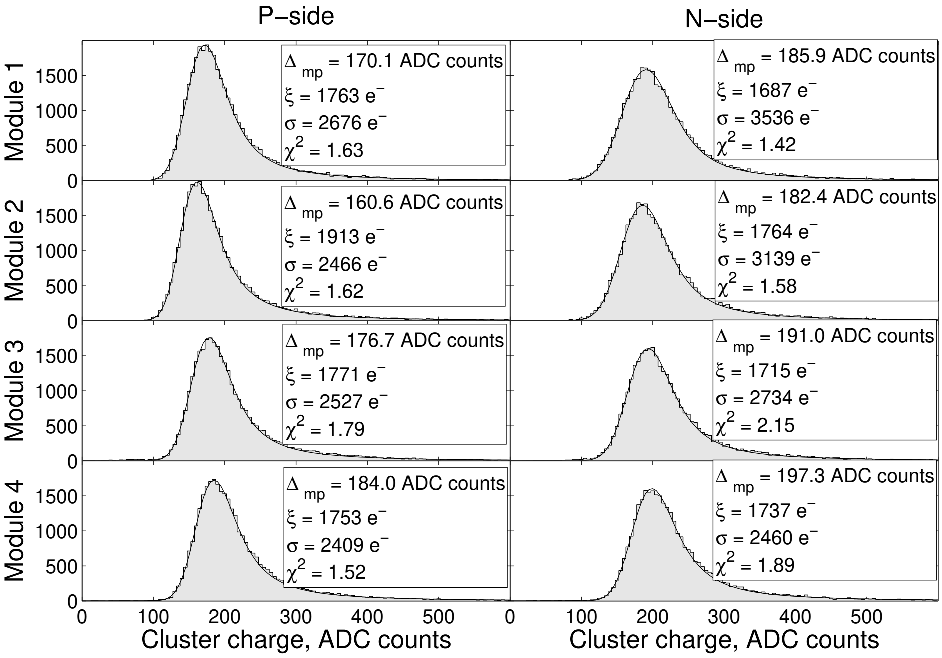

Fig. 3. The distribution of the cluster charge fitted with Landau function (adapted from CERNLIB routine DENLAN) folded with a Gaussian function. The fit parameter $\Delta_{\mathrm{mp}} = 25000\ e^-$ is the most probable charge deposition given by the Landau function and is used for the calibration of the ADC scale. The parameter ξ is the measure FWHM of Landau distribution and σ_{Gauss} is the standard deviation of the Gaussian function.

Table 1
Signal-to-noise ratio of the modules.

Module number	Median strip noise, e^-		S/N ratio	
	P-side	N-side	P-side	N-side
1	435	1487	57	18
2	435	1415	56	18
3	354	559	70	45
4	331	575	75	43

finite charge resolution and a broadening of the charge deposition distribution for thin absorbers [10,11].

The signal-to-noise ratio for all modules is summarized in table 1. The signal-to-noise ratio is defined as the most probable value of the ratio S_{Cl}/N_{mean}, where S_{Cl} is the cluster charge and N_{mean} is the mean noise of the cluster strips. A relatively low S/N ratio on the N-side of the modules 1 and 2 is due to roughly three times higher noise on the N-side of these modules.

A good matching between the cluster charge collected by P- and N-sides is

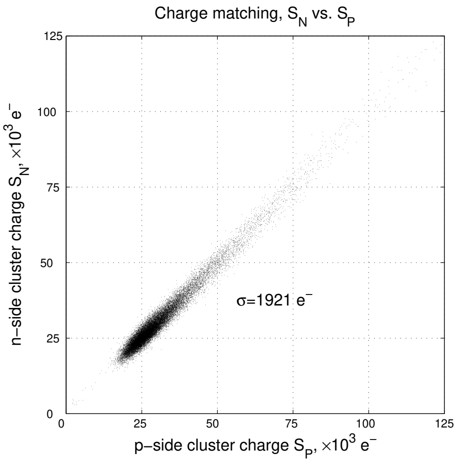

Fig. 4. Correlation between P-side cluster charge S_P and N-side cluster charge S_N, module 4.

Module	R.M.S. of $S_P - S_N, e^-$	
number	Measured	Estimated
1	2549	1846
2	2667	1884
3	1760	995
4	1921	969

Table 2. The measured σ_corr, compared to $(\sigma_\mathrm{corr})_{l.l.}$.

essential for the hit reconstruction in the high-multiplicity events. The figure 4 shows the correlation of the P-side cluster charge S_P and the N-side cluster charge S_N obtained in the single-particle events for module 4. The quality of the charge matching can be characterized by the r.m.s. of the difference between S_P and S_N:

$$\sigma^2_\mathrm{corr} = \frac{1}{n}\sum_{i=1}^{n}[(S_\mathrm{P})_i - (S_\mathrm{N})_i]^2 \qquad (4)$$

The lower limit of σ_corr can be obtained from the detector strip noise data as:

$$(\sigma^2_\mathrm{corr})_{l.l.} = \frac{1}{n}\sum_{i=1}^{n}[(N_{Cl,\mathrm{P}})^2_i + (N_{Cl,\mathrm{N}})^2_i] \qquad (5)$$

where $(N_{Cl})_i$ is the cluster noise in the event i and the summation is done over all the considered events. The lower limit and the actual σ_corr are listed in the table 2. The actual σ_corr obtained from the data are 1.2-1.7 times bigger then the cluster noise estimates $(\sigma_\mathrm{corr})_{l.l.}$. This can be attributed to the occasional loss of a fraction of the cluster charge in the cases when the charge is shared between two strips. If the most of the charge goes to one strip, then the fraction of the signal collected by the neighboring strip is taken into account only if it exceeds S/N cut, which leads to an underestimation of the cluster charge in this case (unless all the signal really goes to one strip). Since this happens on P- and N-sides independently, it increases the difference between P- and N-side measured charge.

3.3 Alignment

In order to benefit from the high intrinsic spatial resolution of the detectors, one has to know the exact location of the sensors of the telescope. The approximate position of the sensors is known to the precision of ≈ 1 mm from the design of the detector holders, and the small corrections that determine the actual position can be measured by studying particle track fit residuals. The algorithm of aligning the detectors by particle tracks described in [12] was used here. Following this algorithm the alignment of the two inner sensors with respect to the outer two was made. Three alignment parameters for each of the two inner sensors were determined: the horizontal offset Δu along the longer sensor edge, the vertical offset Δv along the shorter edge and the rotation angle $\Delta\gamma$ around the beam axis Z. The method consists of fitting a straight track to the two outer sensors and finding the position of the inner sensors which minimizes the global fit χ^2_{Glob} for each sensor. Very few iterations were required to reach the convergence of all alignment parameters. Using 14000 tracks the obtained precision of the alignment parameters was much better than the sensor intrinsic resolution.

3.4 Spatial Resolution

The sensor intrinsic position resolution can be estimated by fitting a track to the reconstructed hits and investigating the residuals. There exist several methods of how to obtain it from the distributions of the residuals [13]. In the first method, a straight track is fitted to the reference sensors and then extrapolated to the studied sensor. Since the studied sensor is not included in the fit, the dispersion of the fit residuals σ^2_r is just a sum of the squared sensor intrinsic spatial resolution σ^2_{intr} and squared track fit error σ^2_f, hence:

$$\sigma^2_{intr} = \sigma^2_r - \sigma^2_f \tag{6}$$

In the other method the studied sensor is included in the fit, and then one has to include the correlation term which leads to:

$$\sigma^2_{intr} = \sigma^2_r + \sigma^2_f \tag{7}$$

In both cases one needs to know the fit error σ_f which is defined by the geometrical arrangement of the modules along the beam axis and by the intrinsic resolutions of the modules σ_{intr} – the values we are looking for and which are not known beforehand. One has to make an initial assumption on the resolutions and then solve the problem iteratively.

We will make an attempt to use here a different method that requires no iterations. We consider an unweighted straight line fit to all four modules and establish the relation between the observed fit residuals and the sensor measurement errors. From the formalism of the method of least-squares one can obtain this relation in the linear form:

$$\langle \boldsymbol{\epsilon}^2 \rangle = \mathbf{B}^I \cdot \langle \mathbf{r}^2 \rangle. \tag{8}$$

where $\langle \boldsymbol{\epsilon}^2 \rangle$ is the column four-element vector of the squared intrinsic resolutions defined as the dispersions of the sensor measurement errors ϵ, $\langle \mathbf{r}^2 \rangle$ is the vector of the observed dispersions of the fit residuals and $\mathbf{B}^I$ is the pseudoinverse of the 4×4 matrix $\mathbf{B}$ which depends only on the z-coordinates of the sensors. The derivation and the caveats of the matrix inversion method are given in the appendix of this paper.

For the spatial resolution measurements we kept the events with one and only one hit in each sensor. The unweighted least squares fit with straight tracks to the four hit points was done independently for x and y coordinates. The unweighted fit minimizes the sum of squared residuals for each track:

$$s_x^2 = \sum_{i=1}^{4} r_{i,x}^2 = \sum_{i=1}^{4} (x_{\mathbf{m},i} - x_{\mathbf{f},i})^2 \tag{9}$$

$$s_y^2 = \sum_{i=1}^{4} r_{i,y}^2 = \sum_{i=1}^{4} (y_{\mathbf{m},i} - y_{\mathbf{f},i})^2 \tag{10}$$

where $x_{\mathbf{m},i}$ and $y_{\mathbf{m},i}$ are the x and y hit coordinates measured by i-th module; $x_{\mathbf{f},i}$ and $y_{\mathbf{f},i}$ are the fitted track impact points; $r_{i,x}$ and $r_{i,y}$ are the fit residuals. The variances of the fit residual distributions, which are used for the calculation of the spatial resolutions, are sensitive to the shape of the tails of the distributions. If a particle gets scattered by a significant angle in one of the two inner sensors (the scattering in the outer two plays no role because the directions of the incoming and outgoing particles are not measured), then the straight line fit to a real kinked track would result in large residuals in all four sensors, hence in larger values of s_x and s_y. A cut on s_x and s_y may thus effectively remove these events from the analysis and suppress the influence of the multiple scattering by large angles on the final results. The distribution of s_x is shown on figure 5. The effect of different s_x^{cut} on the spatial resolution calculated according to eq. (26) is demonstrated on figure 6. The cut values s_x^{cut} and s_y^{cut} are chosen such that they remove the non-gaussian tails of the residual distributions (especially prominent for x-residuals where the spatial resolution is high) but practically do not affect the core (see the pulls distribution on fig. 8). The chosen value s_x^{cut} discards $\approx 2.5\%$ of the events.

The spatial resolution results are shown on the fig.7. In order to compare the above described method with the more commonly used iterative method, the

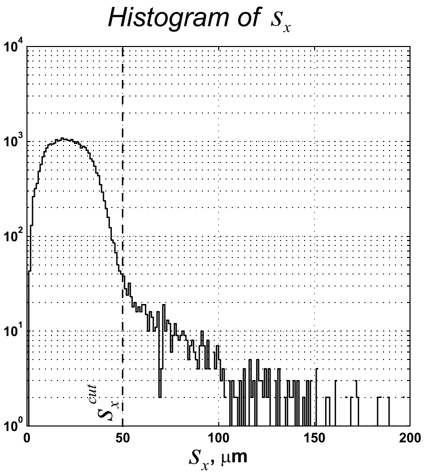

Fig. 5. The distribution of s_x. The cut on s_x rejects the tracks with large kinks due to multiple scattering. With s_x^{cut}=50 μm, 2.5% of events are rejected.

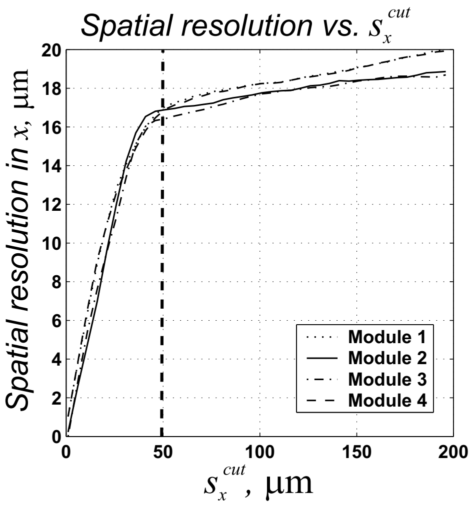

Fig. 6. The effect of s_x^{cut} on the spatial resolution measurement.

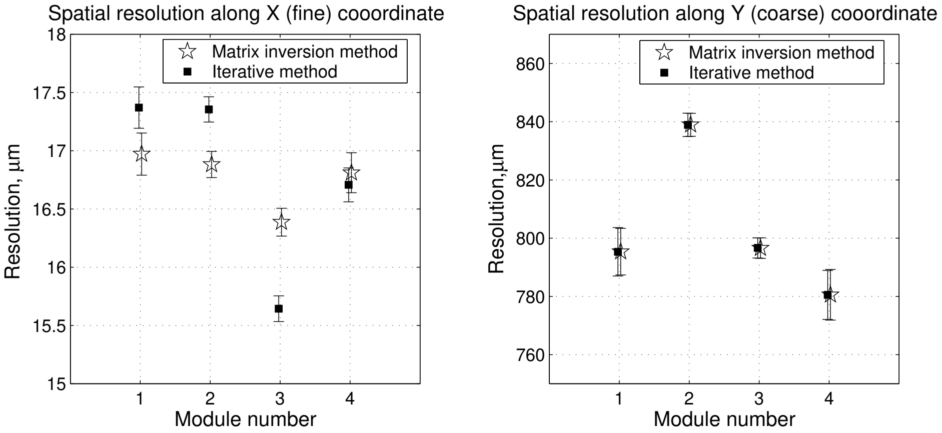

Fig. 7. The sensor intrinsic position resolution. The results from both the iterative method and the matrix inversion methods are shown.

results of the later are also shown on the same plot. One can see that for the position resolution along the coarse coordinate y, both methods produce practically identical results, although the matrix inversion method does it in one step. The results for the fine coordinate x are also rather close albeit not identical because of the measurement error correlations caused by multiple scattering. In the absence of multiple scattering both methods would give the same answer. Both methods result in an average spatial resolution of $\approx$ 17 μm in x-direction and $\approx$ 800 μm in y-direction. The errorbars shown on the picture represent the statistical errors, the systematical uncertainty is estimated to be of the order $\approx$ 1 μm for x-coordinate and $\approx$ 30 μm for y-coordinate due to the uncertainty of s_x^{cut} and s_y^{cut} values and the neglected correlation in the measurement errors.

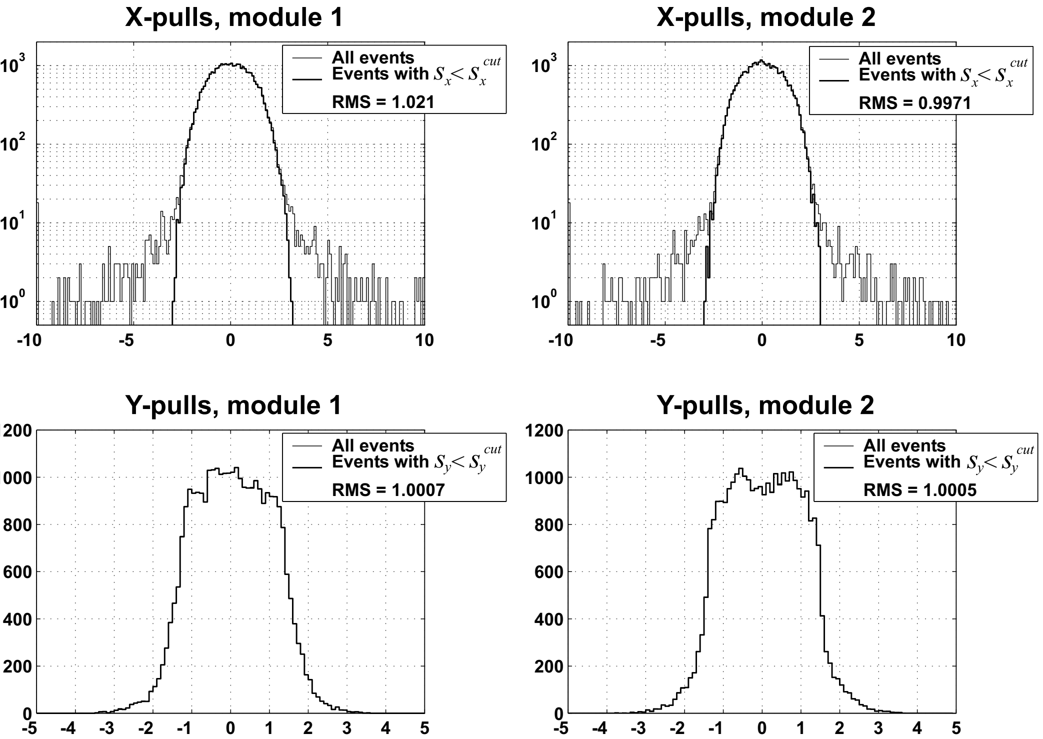

Fig. 8. p_x and p_y pulls for the first two modules.

The fit pull distributions can be used to cross-check the correctness of the obtained result. For a particular module the pull functions $p_\mathbf{x}$ and $p_\mathbf{y}$ are determined as the weighted fit residuals normalized to their standard deviations estimated from the sensors spatial resolutions:

$$p_\mathbf{x} = \frac{x_\mathbf{m} - x_\mathbf{f}}{\sqrt{\sigma_{intr}^2 - \sigma_f^2}} \tag{11}$$

The fit errors σ_f are obtained from least squares fit formalism using error propagation of the errors on slope and intercept. The figure 8 demonstrates the fit pull distributions for the modules 1 and 2 obtained using the fit weights equal to the inverse of the sensor spatial resolutions. The standard deviations are close to unity, as expected from the equation (11).

3.5 Efficiency

The module efficiency is defined as the probability of detecting a charged particle if it passes through the sensor sensitive area. Let's denote the i-th module as a "test module" and all others as "reference modules". The efficiency ε_i of the module i in the telescope can be measured as a ratio of the number of events where all four modules detected a hit over a number of events where

Table 3
Module efficiency

Module	P-side efficiency, %	N-side efficiency, %	Total efficiency ε, %
1	99.76 ± 0.03	99.17 ± 0.05	98.97 ± 0.09
2	99.81 ± 0.02	99.34 ± 0.05	98.34 ± 0.07
3	99.16 ± 0.05	99.61 ± 0.04	98.84 ± 0.09
4	99.71 ± 0.03	99.89 ± 0.02	99.57 ± 0.06

either only the reference modules or all four modules detected a hit:

$$\varepsilon_i \simeq \frac{N_{all}}{N_{ref} + N_{all}} \tag{12}$$

or in other words $1 - \varepsilon_i$ is a chance that the i-th module misses a particle hit. In order to determine ε_i, the tracks found using only the three reference modules were inter- or extrapolated to the test module. In order to make sure that the particle track really passed through the test sensor's sensitive area, we kept only those events where the projected impact point lied at least 5 mm away from the sensor edge in y-direction and 200 μm in x-direction. The region around the projected impact point was searched for the hits and the hit was accepted if it was found closer then 300 μm in x-direction and 7500 μm in y-direction from the extrapolated impact point. These cut values were selected after studying the distribution of the residuals and were chosen such to include also the events were the particle was deflected off the trajectory due to multiple scattering or δ-ray production. The chance of finding a noise cluster inside this region is negligible since the probability of having a noise cluster per sensor side is less than 1%. The results of the efficiency calculation with statistical errors are shown in the table 3.

It's illustrative to plot the expected location of the missing hits in the test module using the tracks reconstructed from the reference modules. It was found that the missing hits are not randomly scattered across the sensor area but are concentrated along the noisy or dead strips of the module (see fig. 9). The disconnected strips seem not to cause a particle loss as long as these strips are not clustered together. The particle loss is thus a direct consequence of the module production defects. The efficiency of the module areas with nominal strip noise and absence of bonding defects is consistent with 100%.

4 Conclusion

In this paper we have presented results from the tests, with 7 GeV/c pion beam, of four double-sided silicon strip detectors of ALICE SSD design.

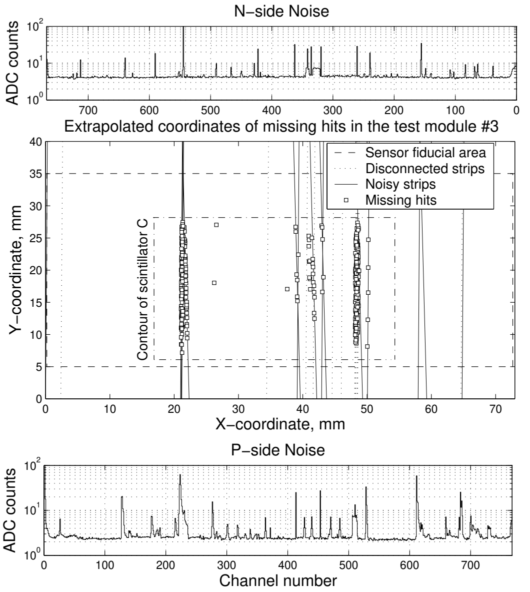

Fig. 9. Location of the missing hits on the module 3. The trigger scintillator C selects only the middle part of the sensor. The missing hits are located along the noisy strips or disconnected strips clustered together.

It was demonstrated that the module design provides excellent signal to noise ratios in the range 40-75. The higher noise level found on the N-side of the sensors of one of the manufacturers was discussed with the manufacturer and has been corrected before the final production. The cause of the higher noise was a high interstrip capacitance, which has been decreased in the final sensor design, so that the noise level on the N-side decreased practically to the noise level of the P-side.

The good performance of the sensors and the front-end electronics results in a high detection efficiency for minimum ionizing particles, typically 99.5% per sensor side or 98.9% for both in coincidence.

A fast method for determination of the spatial resolution was developed. It was shown that a measurement with four unknown detectors, without a reference telescope, can still be analyzed assuming that the four detectors have similar (but not necessarily exactly equal) spatial resolution. The four ALICE SSD modules were shown to provide a resolution of 17 μm in the x-direction and 800 μm in the y-direction. Since the clustering algorithm used here exploits the information provided by the charge sharing between neighboring strips, these resolutions are better then the digital resolution expected for the 95 μm strip pitch, which would already be sufficient for ALICE experiment.

5 Appendix

Let's consider a least squares straight line fit to the hit points in all the modules in the telescope and establish a connection between the observed dispersion of the fit residuals and the sensor measurement errors. The weights of all the points of the fit are kept equal to avoid the recursiveness of the problem. We follow the matrix formalism of the least squares method described for example in [14]. Let's denote $\mathbf{z} = (z_1, \dots, z_n)^T$ as the coordinates of the n sensor planes along the beam axis Z, and $\mathbf{x_m} = (x_{\mathbf{m},1}, \dots, x_{\mathbf{m},n})^T$ as the hit coordinates measured by the sensors in the particular event and projected on the plane XZ or YZ (see fig.1). The measurement errors $\boldsymbol{\epsilon} = (\epsilon_1, \dots, \epsilon_n)^T$ are defined as the difference between the measured hit coordinates $\mathbf{x_m}$ and the real particle track impact points $\mathbf{x_t}$:

$$\mathbf{x_m} = \mathbf{x_t} + \boldsymbol{\epsilon} \tag{13}$$

The sensor intrinsic position resolution is defined as the r.m.s. of the measurement errors: $\sigma^2_{intr,i} \equiv \langle \epsilon_i^2 \rangle$.

Considering the particle track as a straight line we can rewrite eq. (13) in the following form:

$$\mathbf{x_m} = \mathbf{Z} \cdot \boldsymbol{\beta} + \boldsymbol{\epsilon}, \tag{14}$$

where $\mathbf{Z}$ is a design matrix and $\boldsymbol{\beta}$ is a vector of coefficients :

$$\mathbf{Z} = \begin{bmatrix} 1 & z_1 \\ 1 & z_2 \\ \vdots & \vdots \\ 1 & z_n \end{bmatrix}; \qquad \boldsymbol{\beta} = \begin{bmatrix} \beta_0 \\ \beta_1 \end{bmatrix}$$

Values β_0 and β_1 are the track intercept and slope respectively. The effect of multiple scattering in the sensor material makes the real particle trajectory slightly kinked, so that the parameters β_0 and β_1 serve only as a straight track approximation to the real particle trajectory. With this approximation the effect of multiple scattering will contribute to the measurement errors. The scattering angle distribution has a gaussian core which contains 98% of all the events, and long non-gaussian tails extending far outside several standard deviations. For pions with momentum of 7 GeV/c and a spacing between the sensors of 3 cm the r.m.s. deviation of the particle track in the next sensor plane due to multiple scattering in the previous sensor plane is about 2.5 μm, which is a small number compared to the expected resolution of ≈ 18 μm in the x-direction if the numbers are added in quadrature, and totally negligible compared with the resolution of 800 μm in the y-direction. However, the non-gaussian tails of the distribution can not be neglected in our case. Events with large scattering angle were excluded from the analysis, as will be explained later in this section.

The fitted track impact points $\mathbf{x_f} = (x_{\mathbf{f},1}, \ldots, x_{\mathbf{f},n})^T$ are determined as:

$$\mathbf{x_f} = \mathbf{H} \cdot \mathbf{x_m} \tag{15}$$

where

$$\mathbf{H} = \mathbf{Z}(\mathbf{Z}^T\mathbf{Z})^{-1}\mathbf{Z}^T. \tag{16}$$

The fit residuals $\mathbf{r} = \mathbf{x_m} - \mathbf{x_f}$ are given by:

$$\mathbf{r} = (\mathbf{I} - \mathbf{H}) \cdot \mathbf{x_m}. \tag{17}$$

where $\mathbf{I}$ is an $n \times n$ unitary matrix. Plugging eq.(14) into eq.(17) and noting that

$$(\mathbf{I} - \mathbf{H}) \cdot \mathbf{Z} = 0 \tag{18}$$

one obtains the relationship between the fit residuals and the measurement errors:

$$\mathbf{r} = (\mathbf{I} - \mathbf{H}) \cdot \boldsymbol{\epsilon}. \tag{19}$$

The matrix $(\mathbf{I} - \mathbf{H})$ depends only on the position of the modules along Z axis and does not depend on the data. The rank of this matrix is $n - 2$ since there are only $n - 2$ independent residuals. Assuming that there is no correlation between the measurement errors in different sensors:

$$\text{cov}(\epsilon_i, \epsilon_j) = 0,\ i \neq j, \tag{20}$$

one can make a step from $\boldsymbol{r}$ and $\boldsymbol{\epsilon}$ to their r.m.s values and obtain the linear relationship between the dispersions of the fit residuals $\langle r_i^2 \rangle$ and the squared sensor intrinsic resolutions $\langle \epsilon_i^2 \rangle$:

$$\langle \mathbf{r}^2 \rangle = \mathbf{B} \cdot \langle \boldsymbol{\epsilon}^2 \rangle, \tag{21}$$

where matrix $\mathbf{B}$ is obtained by squaring the elements of $(\mathbf{I} - \mathbf{H})$:

$$B_{ij} = (\delta_{ij} - H_{ij})^2. \tag{22}$$

As well as $\mathbf{H}$, the matrix $\mathbf{B}$ also depends only on the position of the modules along Z axis. If the matrix $\mathbf{B}$ is nonsingular, then the system of linear equations (21) can be solved, and one obtains, without any iterations, the vector of squared intrinsic resolutions $\langle \boldsymbol{\epsilon}^2 \rangle$ using the inverse of the matrix $\mathbf{B}$:

$$\langle \boldsymbol{\epsilon}^2 \rangle = \mathbf{B}^{-1} \langle \mathbf{r}^2 \rangle. \tag{23}$$

It is easy to show[7] that the matrix $\mathbf{B}$ is nonsingular only if $n \geqslant 5$, which means that $n = 5$ is the *minimal* number of sensors in the telescope, with

---

[7] Using the fact that the rank of the matrix $\mathbf{I} - \mathbf{H}$ is $n - 2$

which the resolution of each of them can be unambiguously determined using eq. (23).

In our case $n = 4$ and rank($\mathbf{B}$) = 3, therefore $\mathbf{B}^{-1}$ does not exist and there is no unique solution to the equation (21) which becomes underdetermined. Instead, if the vector $\langle \mathbf{r}^2 \rangle$ belongs to the rangespace of the matrix $\mathbf{B}$, which is the case when the eq. (20) holds, there exists a family of solutions each of which satisfies the equation (21). The family of solutions can be described as:

$$\langle \boldsymbol{\epsilon}^2 \rangle = \langle {\boldsymbol{\epsilon}_\mathbf{0}}^2 \rangle + \alpha \cdot \mathbf{V_0} \tag{24}$$

where $\langle {\boldsymbol{\epsilon}_\mathbf{0}}^2 \rangle$ is the particular solution, $\mathbf{V_0}$ – the null-space of the matrix $\mathbf{B}$ (the eigenvector that corresponds to the zero eigenvalue) and α is a free parameter. If no other information is available on the sensor resolutions or their ratios, then there is no preference in choosing a particular parameter α [8] . But if, as is often the case, all the sensors in the telescope are similar, then a reasonable choice would be to pick a solution which gives the closest values for all the sensors. In the general case, to find such a solution one has to find a point on a line in a 4-D space represented by the equation (24), which is the closest to the skew line given by the equation:

$$\mathbf{s} = \mathbf{n} \cdot \tau, \text{ where the vector } \mathbf{n} = (1,1,1,1), \text{ and } \tau \text{ is a free parameter.} \tag{25}$$

In case of a symmetric arrangement of the modules around the middle plane of the telescope (like in our setup), this is equivalent to minimizing the norm of the vector $\langle \boldsymbol{\epsilon}^2 \rangle$. This solution can be obtained by multiplying the vector $\langle \mathbf{r}^2 \rangle$ by a matrix $\mathbf{B}^I$ pseudoinverse to $\mathbf{B}$:

$$\langle \boldsymbol{\epsilon}^2 \rangle_{min} = \mathbf{B}^I \cdot \langle \mathbf{r}^2 \rangle. \tag{26}$$

The vector $\langle \boldsymbol{\epsilon}^2 \rangle_{min}$ also belongs to the family of solutions given by the eq. (24) but has the smallest norm $\|\langle \boldsymbol{\epsilon}^2 \rangle\|$.

The introduction of multiple scattering creates certain correlations between the measurement errors in different sensors and as a result eq. (21) holds only approximately. For $n \geqslant 5$ the solution of this equation always exists, but for $n = 4$ it can be solved only in the least-squares sense, which means finding a solution $\langle \boldsymbol{\epsilon}^2 \rangle$ that minimizes the norm $\|\mathbf{B} \cdot \langle \boldsymbol{\epsilon}^2 \rangle - \langle \mathbf{r}^2 \rangle\|$, or in other words, best explains the observed dispersions of fit residuals. Such a solution is again given by the eq. (26) and it was used in the current data analysis.

---

[8] Of course, α can only be chosen such that the squared resolutions $\langle \boldsymbol{\epsilon}^2 \rangle$ remain positive.

References

[1] CERN LHCC 99-12, ALICE ITS Technical Design Report,

[2] P. Kuijer et al., “The Inner Tracking System of the Alice Experiment”, Nucl. Instr. and Meth. **A**530 (2004) 28.

[3] CERN/LHCC 95-71, ALICE Technical Proposal,

[4] J.Kemmer, G.Lutz et al., “New structures for position sensitive semiconductor detectors”, Nucl. Instr. and Meth. **A**273 (1988) 588-598

[5] C. Hu-Guo, Proceedings of the 8th Workshop on Electronics for LHC Experiments, Colmar, France, October 2002.

[6] A.P.deHaas *et al.*, “Aluminium Microcable Technology for ALICE Silicon Strip Detector: A Status Report”, proceedings of 8th Workshop on Electronics for LHC Experiment, Colmar, France, October 2002

[7] R.Kluit *et al.*, “Realization of ladder EndCap electronics for the ALICE ITS SSD. Proceedings of 10th workshop on electronics for LHC and future experiments. Boston, USA, September 2004.

[8] Phys. Rev. **D54**, Part 1, “Particle detectors”, 145 (1996).

[9] L.Landau, “On the energy loss of fast particles by ionization”. J. Physics USSR Vol. VIII, 4 (1944)

[10] S.Hancock et.al., “Energy loss and energy straggling of protons and pions in the momentum range 0.7 to 115 GeV/c”, Phys. Rev., A28, 1983.

[11] J.F.Bak et.al.,“Large Departures from Landau Distributions for High-Energy Particle Travesing Thin Si and Ge Tragets”, Nuclear Physics B288 (1987) 681-716.

[12] V.Karimäki, A.Heikkinen, T.Lampén, T.Lindén, “Sensor Alignment by Tracks”, *CHEP03*, La Jolla California; arXiv:physics/0306034.

[13] V.Karimäki et al., Nucl. Instr. and Meth. **A**453 (2000) 536.

[14] Draper, N.R and H. Smith, Applied Regression Analysis, 3rd Ed., John Wiley & Sons, New York, 1998.